

Quasi-classical description of molecular dynamics based on Egorov's theorem

Johannes Keller^{1, a)} and Caroline Lasser^{1, b)}

Zentrum Mathematik, Technische Universität München

Egorov's theorem on the classical propagation of quantum observables is related to prominent quasi-classical descriptions of quantum molecular dynamics as the linearized semiclassical initial value representation (LSC-IVR), the Wigner phase space method or the statistical quasiclassical method. The error estimates show that different accuracies are achievable for the computation of expectation values and position densities. Numerical experiments for a Morse model of diatomic iodine and confined Henon–Heiles systems in various dimensions illustrate the theoretical results.

PACS numbers: 82.20Ln, 82.20Wt

Keywords: quasi-classical propagation, molecular dynamics, Wigner function, linearized semiclassical initial value representation

I. INTRODUCTION

The numerical simulation of quantum molecular dynamics is a notoriously difficult problem, since the key equation, the vibrational time-dependent Schrödinger equation, is a partial differential equation on a high dimensional configuration space with solutions, that oscillate in time and space.

Over decades this challenge has been tackled by methods that directly compute quantities of physical interest without solving the Schrödinger equation or fully discretizing its unitary propagator. The linearized semiclassical initial value representation (LSC-IVR)^{1–3}, for example, approximates time-dependent correlation functions and expectation values by initial phase space sampling and classical trajectory calculations. The Wigner phase space method^{4–6} and the statistical quasiclassical method⁷ similarly approximate time-dependent transition probabilities.

A unifying property of these quasi-classical approaches is the following three-step procedure: (i) Sampling of an initial phase space density (ii) Classical propagation of the sampling

points (iii) Weighted summation over the time-evolved phase space points. Notably the second and third algorithmic step are numerically more favorable than solving the time-dependent Schrödinger equation in higher dimensions. Often the computational times are in the range of seconds.

Quasi-classical methods are well-established in the literature and have been thoroughly discussed also with respect to deficiencies for quantum coherence on longer time scales^{3,8} or zero point energy leakage⁹. They have been derived from the asymptotic expansion of the Wigner transformed Schrödinger equation⁴, semiclassical initial value representations⁸ and the path integral formulation^{10,11} of the unitary propagator.

Our aim here is to add a complementary derivation by relating quasi-classical algorithms to Egorov's theorem^{12,13} on the classical propagation of quantum observables. Moreover, Egorov's theorem also implies error estimates for the computation of time-evolved expectation values and position densities. In all cases, the error crucially depends on the time evolution of derivatives of the classical trajectories with respect to their initial data. But more can be inferred: One assumes that the vibrational

^{a)}keller@ma.tum.de

^{b)}lasser@ma.tum.de

Schrödinger operator can be written as

$$\widehat{H} = -\frac{\varepsilon^2}{2}\Delta + V, \quad (1)$$

where ε is a small positive parameter and V a potential energy surface (PES). Then, time-dependent expectation values are approximated with an error of the order ε^2 for all initial states with $\langle \psi | \psi \rangle = 1$. The approximation of position densities and transition probabilities, however, requires localization assumptions on the initial state, and in typical vibrational situations one can only expect an error of the order $\sqrt{\varepsilon}$.

We proceed as follows: In §II we present Egorov's theorem together with estimates for the time-dependence of the error. In §III we relate Egorov's theorem to the linearized semiclassical initial value representation (LSC-IVR) and the Wigner phase space method. §IV discusses the computational tasks of quasi-classical algorithms. In §V we present numerical experiments for a Morse-model of diatomic Iodine and confined Henon–Heiles systems ranging from dimension 2 to 32. §VI summarizes our results, while the Appendices collect elements of our theoretical error analysis.

II. VIBRATIONAL QUANTUM DYNAMICS

A. Unitary propagator

Within the framework of the Born–Oppenheimer approximation, the Schrödinger operator for effective one-level nuclear quantum dynamics writes in atomic units as

$$\widehat{H} = -\sum_{j=1}^d \frac{1}{2m_j} \Delta_{q_j} + V,$$

where m_j is the mass for the j th component of the nuclear coordinate vector. The real-valued function $V : \mathbb{R}^d \rightarrow \mathbb{R}$ is a potential energy surface (PES) of the molecular system.

Setting

$$\varepsilon = 1/\sqrt{\max(m_1, \dots, m_d)}$$

and scaling the coordinates according to $q_j \mapsto q_j/(\varepsilon\sqrt{m_j})$, we write the Schrödinger operator in the semiclassical form (1) and study the vibrational dynamics on the macroscopic time scale, that is, we use the time-scaled unitary propagator

$$U_t = e^{-i\widehat{H}t/\varepsilon}.$$

Depending on the nuclear masses, the scale parameter ε ranges between 10^{-3} and 10^{-2} . For example, the diatomic iodine molecule considered later on has $\varepsilon = 0.0122$, and accordingly one unit of the macroscopic time scale corresponds to 1.98 femtoseconds.

B. Observables

The observables result from the Weyl quantization of functions $A : \mathbb{R}^d \times \mathbb{R}^d \rightarrow \mathbb{C}$ according to

$$\begin{aligned} (\widehat{A}\psi)(q) &= \\ (2\pi\varepsilon)^{-d} \int A\left(\frac{1}{2}(q+y), p\right) e^{i(q-y)\cdot p/\varepsilon} \psi(y) dp dy, \end{aligned}$$

where $\psi : \mathbb{R}^d \rightarrow \mathbb{C}$ is a square-integrable function. The ε -scaling of the Fourier term allows to view the Schrödinger operator \widehat{H} as the quantization of the ε -independent energy function

$$H(q, p) = \frac{1}{2}|p|^2 + V(q). \quad (2)$$

Also the position and momentum operators $\psi \mapsto q_j\psi$ and $\psi \mapsto -i\varepsilon\partial_j\psi$ for $j = 1, \dots, d$ originate from the ε -independent phase space functions $(q, p) \mapsto q_j$ and $(q, p) \mapsto p_j$, respectively.

For the trace of two Weyl quantized observables one has the beautiful integral formula

$$\text{tr}(\widehat{A}\widehat{B}) = (2\pi\varepsilon)^{-d} \int A(z)B(z)dz.$$

C. Wigner functions

Expectation values for Weyl quantized observables can be expressed in terms of the

Wigner function $W_\psi : \mathbb{R}^d \times \mathbb{R}^d \rightarrow \mathbb{R}$,

$$W_\psi(q, p) = (2\pi\varepsilon)^{-d} \int \psi(q - \frac{1}{2}y) \psi^*(q + \frac{1}{2}y) e^{ip \cdot y/\varepsilon} dy,$$

via

$$\langle \psi | \widehat{A} | \psi \rangle = \int A(z) W_\psi(z) dz.$$

Moreover, the Weyl quantization of the Wigner function W_ψ is the projector for ψ ,

$$(2\pi\varepsilon)^d \widehat{W}_\psi = |\psi\rangle\langle\psi|.$$

A typical initial state for vibrational quantum dynamics is the ground state of an harmonic oscillator $\widehat{H} = -\frac{\varepsilon^2}{2}\Delta + \frac{1}{2}|q|^2$, or slightly more general, a localized Gaussian wavepacket with phase space center $z_0 = (q_0, p_0)$,

$$\psi(q) = (\det(\Sigma)/\pi\varepsilon)^{d/4} \exp\left(\frac{i}{\varepsilon} p_0 \cdot (q - q_0)\right) \times \exp\left(-\frac{1}{2\varepsilon} (q - q_0) \cdot \Sigma (q - q_0)\right), \quad (3)$$

where $\Sigma \in \mathbb{R}^{d \times d}$ is a positive definite diagonal matrix with entries $\sigma_1, \dots, \sigma_d$. Its Wigner function is given by

$$W_\psi(z) = (\pi\varepsilon)^{-d} \exp\left(-\frac{1}{\varepsilon} (z - z_0) \cdot \Sigma_2 (z - z_0)\right), \quad (4)$$

where $\Sigma_2 \in \mathbb{R}^{2d \times 2d}$ is the diagonal matrix with diagonal entries $\sigma_1, \dots, \sigma_d, 1/\sigma_1, \dots, 1/\sigma_d$.

In contrast to the Gaussian wavepacket (3), most Wigner functions attain negative values. The Wigner functions of the Hagedorn wavepackets or the generalized squeezed states, for example, can be expressed as the product of a Gaussian and a Laguerre polynomial¹⁴. In general, however, analytical formulas are not available, and Wigner functions have to be computed numerically, which poses a very difficult problem of high-dimensional oscillatory numerical integration.

D. Egorov's theorem

Quasi-classical approximations rely on the flow $\Phi_t : \mathbb{R}^{2d} \rightarrow \mathbb{R}^{2d}$ of the classical Hamiltonian function (2). The flow relates initial

phase space points (q_0, p_0) with their location at time t . One has $\Phi_t(q_0, p_0) = (q_t, p_t)$ with

$$\dot{q}_t = p_t, \quad \dot{p}_t = -\nabla V(q_t). \quad (5)$$

Egorov's theorem^{12,13} proves for the propagation of Weyl quantized observables that

$$U_{-t} \widehat{B} U_t = \widehat{B \circ \Phi_t} + \varepsilon^2 E(V, B, \Phi_t) \quad (6)$$

holds, where the error term $E(V, B, \Phi_t)$ depends on the following:

- (i) potential derivatives $\partial^\alpha V$ with $|\alpha| \geq 3$,
- (ii) observable-flow derivatives $\partial^\alpha (B \circ \Phi_t)$ with $|\alpha| \geq 1$,

see Appendix A. If the potential V is a polynomial of degree less or equal than two, then $E(V, B, \Phi_t) = 0$, and the classical propagation of observables exactly describes the quantum evolution. Moreover, if $B = H$, then $E(V, H, \Phi_t) = 0$ as well.

E. Ehrenfest time

For the analysis of Egorov's theorem (cf. Ref.¹³ and Appendix A), the derivatives of the classical Hamiltonian flow are crucial. The worst case estimate gives for any multi-index $\alpha \in \mathbb{N}^{2d}$ a constant $C_\alpha > 0$ such that for all $t \in \mathbb{R}$ and $z \in \mathbb{R}^{2d}$

$$|\partial^\alpha \Phi_t(z)| \leq C_\alpha e^{\Gamma|\alpha| \cdot |t|}, \quad (7)$$

where the flows's stability indicator $\Gamma > 0$ is related to the eigenvalues of the Hessian matrix $D^2V(q)$ of the potential.

The worst case exponential growth of the flow derivatives (7) implies exponential growth of the error in Egorov's theorem, a phenomenon, which is well-established for nonsymmetric double well potentials¹³. Hence, in the worst case, one has to expect that the ε^2 factor in (6) is consumed after times t of the order $\log(1/\varepsilon)$, the so-called Ehrenfest time scale.

For integrable systems or flows with closed orbits, the exponential estimate (7) can be relaxed to

$$|\partial^\alpha \Phi_t(z)| \leq C_\alpha (1 + |t|)^\alpha,$$

and Egorov's approximation is meaningful until times of the order $1/\sqrt{\varepsilon}$, see Ref.¹³. Our numerical experiments for a model of diatomic iodine and a modified Henon–Heiles system even show persistence on longer time scales.

III. COMPUTATIONAL METHODS

Over decades, quasiclassical approximations in the spirit Egorov's theorem have been used as the backbone for numerical methods in molecular quantum dynamics. We exemplarily summarize two of them.

A. LSC-IVR

The linearized semiclassical initial value representation (LSC-IVR)^{1–3} approximates time-dependent correlation functions by

$$\text{tr}(\widehat{A}U_{-t}\widehat{B}U_t) \approx (2\pi\varepsilon)^{-d} \int A(z)B(\Phi_t(z)) dz,$$

and in particular

$$\begin{aligned} \text{tr}(|\psi\rangle\langle\psi|U_{-t}\widehat{B}U_t) &= \langle U_t\psi | \widehat{B} | U_t\psi \rangle \\ &\approx \int W_\psi(z)B(\Phi_t(z)) dz. \end{aligned}$$

According to the Egorov estimate (6), the LSC-IVR approximates quantum correlation functions and expectation values with an error of the order ε^2 , if the initial state is normalized to $\langle\psi|\psi\rangle = 1$, and if the time-evolved observable originates from Weyl quantizing an ε -independent phase space function B with bounded derivatives¹⁵.

For the approximation of time-evolved position densities, one writes¹⁶

$$\begin{aligned} |(U_t\psi)(r)|^2 &= \langle U_t\psi | \delta_r | U_t\psi \rangle \\ &= (2\pi)^{-d} \int \langle U_t\psi | e^{-i\eta\cdot(q-r)} | U_t\psi \rangle d\eta \\ &\approx \int W_\psi(z)B_\eta(\Phi_t(z)) dz d\eta \end{aligned} \quad (8)$$

with $B_\eta(q, p) = (2\pi)^{-d} e^{-i\eta\cdot(q-p)}$.

For this approximation of $|(U_t\psi)(r)|^2$, the accuracy crucially depends on the initial state ψ . For a vibrational Gaussian wavepacket (3), for example, the approximation error is of the order $\sqrt{\varepsilon}$, see Appendix B and C.

B. Wigner phase space method

The Wigner phase space method^{4–6} and the statistical quasiclassical method⁷ approximate time-dependent transition probabilities as

$$\begin{aligned} |\langle\phi | U_t\psi\rangle|^2 &= \langle U_t\psi | \phi \rangle \langle \phi | U_t\psi \rangle \\ &\approx (2\pi\varepsilon)^d \int W_\phi(\Phi_t(z))W_\psi(z) dz. \end{aligned}$$

Here, Egorov's theorem is used in the form

$$U_{-t}|\phi\rangle\langle\phi|U_t \approx \widehat{B \circ \Phi_t}$$

with $B = (2\pi\varepsilon)^d W_\phi$.

The accuracy of this method depends on the states ϕ and ψ . If they are vibrational states, as for example localized Gaussian wavepackets as defined in Eq. (3), then the third derivatives of the Wigner function contribute terms of the order $\varepsilon^{-3/2}$, such that the overall approximation error is of the order $\varepsilon^{2-3/2} = \varepsilon^{1/2}$, see Appendix C.

IV. COMPUTATIONAL TASKS

For the quasi-classical approximation of expectation values

$$\langle U_t\psi | \widehat{B} | U_t\psi \rangle \approx \int W_\psi(z)B(\Phi_t(z)) dz,$$

the following three computational steps have to be carried out:

(i) Sampling of the initial condition: We choose phase space points $(q_1, p_1), \dots, (q_N, p_N)$ such that

$$\langle \psi | \hat{B} | \psi \rangle \approx \frac{1}{N} \sum_{j=1}^N B(q_j, p_j) \quad (9)$$

for the observables B of interest. This is achieved by Monte Carlo or Quasi-Monte Carlo sampling of the initial Wigner function W_ψ . We note that an unrefined sampling of the initial Husimi function deteriorates the accuracy of the algorithm^{17,18}.

(ii) Classical trajectory calculations: The chosen phase space points are evolved along the trajectories of the corresponding classical Hamiltonian system

$$\dot{q}_t = p_t, \quad \dot{p}_t = -\nabla V(q_t).$$

Since the observables of interest are computed by phase space averaging, these classical equations of motion should be discretized symplectically as e.g. by the Störmer–Verlet method or by higher order symplectic Runge–Kutta schemes, see IV B.

(iii) Evaluation of the observables: At some time t , the algorithm has resulted in phase space points $(q_1(t), p_1(t)), \dots, (q_N(t), p_N(t))$. Then, the expectation values of interest are approximated according to

$$\langle U_t \psi | \hat{B} | U_t \psi \rangle \approx \frac{1}{N} \sum_{j=1}^N B(q_j(t), p_j(t)). \quad (10)$$

A. Phase space sampling and quadrature

We discuss the initial sampling step for Gaussian wave packets of the form (3). Monte Carlo samplings of the corresponding phase space Gaussian (4) can easily be generated by a suitably rescaled and shifted sampling of a standard $2d$ -dimensional Gaussian distribution. The convergence rate of the Monte-Carlo quadrature rule (9) is proportional to $1/\sqrt{N}$, where N is

the number of sampling points. Quasi-Monte Carlo sequences, such as Sobol or Halton sequences, approximate the uniform distribution on the unit cube. To obtain a Gaussian distribution with diagonal covariance matrix, one transforms the uniformly distributed sequences by the cumulative distribution functions of $2d$ univariate Gaussians. The rate of convergence for Quasi-Monte Carlo quadratures is approximately given by¹⁵ $\log(N)^{2d}/N$, and hence deteriorates slightly with increasing dimension.

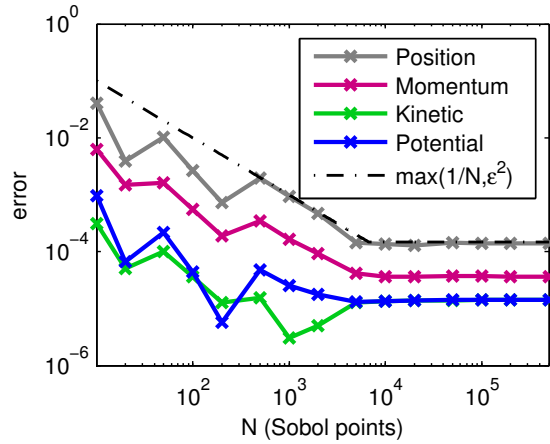


Figure 1. Average errors on the time interval $[0, 166\text{fs}]$ for the one-dimensional Morse system from §V A and different numbers N of Sobol points.

Figure 1 illustrates the numerical convergence of the Sobol quadrature rule (10) when applied to the one-dimensional Morse system from §V A. The errors are averaged over the time interval $[0, 166\text{fs}]$, and we used the Störmer–Verlet scheme with stepsize $\tau = 10^{-3}$ for the dynamics. One observes that the quadrature error is bounded by the maximum of $1/N$ and ϵ^2 , the $1/N$ error originating from the Quasi-Monte Carlo quadrature, the ϵ^2 error originating from the asymptotic approximation of Egorov's theorem.

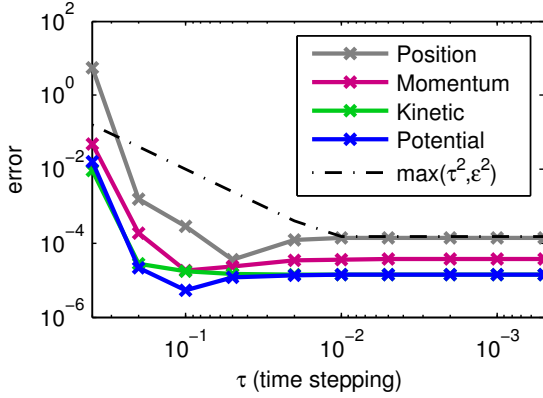


Figure 2. Average errors on the time interval $[0, 166\text{fs}]$ for the one-dimensional Morse system from §V A with different time steppings τ for the Störmer-Verlet integrator.

B. Propagation with symplectic integrators

The most popular symplectic integrator is the Störmer-Verlet scheme which is a symmetric second order method. Its application to the Hamiltonian system (5) with time stepping τ results in the update formula $(q_n, p_n) \mapsto (q_{n+1}, p_{n+1})$ with

$$\begin{aligned} q_{n+1/2} &= q_n + \frac{\tau}{2} p_n \\ p_{n+1} &= p_n - \nabla V(q_{n+1/2}) \\ q_{n+1} &= q_{n+1/2} + \frac{\tau}{2} p_{n+1}. \end{aligned} \quad (11)$$

Higher order symplectic integrators^{19,20} can be constructed by a similar splitting procedure. Figure 2 shows the second order accuracy of the Störmer-Verlet scheme applied to the Morse oscillator from §V A. We used 10^5 Sobol points for the Quasi-Monte Carlo quadrature. Already for moderately small time steppings τ , the ϵ^2 error from the Egorov theorem is dominant.

C. Evaluation of position densities

For the approximation of position densities according to

$$\begin{aligned} |(U_t \psi)(r)|^2 &\approx (2\pi)^{-d} \int W_\psi(z) e^{-i\eta \cdot (q_t - r)} dz d\eta \\ &=: P_t(r), \end{aligned} \quad (12)$$

the previous algorithmic steps (i)–(iii), have to be augmented by an additional quadrature step. This step is, however, only feasible for low dimensional systems:

(iv) Evaluation of the position density: We choose quadrature nodes η_1, \dots, η_M and weights w_1, \dots, w_M such that

$$|(U_t \psi)(r)|^2 \approx \frac{1}{(2\pi)^d N} \sum_{j=1}^N \sum_{k=1}^M e^{-i\eta_k \cdot (q_j(t) - r)} w_k$$

This can be achieved by the Fast Fourier Transform (FFT), since the η -integral defining $P_t(r)$ is an inverse Fourier transform.

V. NUMERICAL EXPERIMENTS

All the experiments presented in this chapter have been performed with MATLAB 8.3 on a 3.33GHz Intel Xeon X5680 processor. The algorithmic structure suggests parallel and GPU computing. Preliminary tests in this direction indicate considerable speed-ups.

A. Ground state dynamics for diatomic Iodine

We first present experiments for the dynamics of a diatomic iodine molecule on the lowest potential energy surface, that is, the electronic ground state of I_2 .

1. The model system

The vibrational degree of freedom is the internuclear distance r , and the electronic ground

state energy is modelled by a Morse potential fitted to experimental data²¹,

$$V_{I_2}(r) = D_e(1 - e^{-\alpha(r-r_e)})^2 \quad (13)$$

with $D_e = 0.0572$ hartree, $\alpha = 0.983a_0^{-1}$, and $r_e = 5.03855a_0$, where the Bohr radius a_0 is unity in atomic units. The associated Schrödinger Hamiltonian

$$\hat{H} = -\frac{1}{2m}\partial_r^2 + V_{I_2}$$

with reduced mass parameter $m = 1.165 \cdot 10^5$ a.u. has previously been used in the literature^{3,22,23}.

To identify the effective semiclassical scale of this model, we set the energy unit to D_e , which yields the rescaled Hamiltonian

$$\hat{H} = -\frac{\varepsilon^2}{2}\partial_r^2 + (1 - e^{-\alpha(r-r_e)})^2$$

with $\varepsilon = \sqrt{1/(mD_e)} = 0.0122$ and the corresponding Schrödinger equation

$$i\varepsilon\partial_t\psi(r, t) = \hat{H}\psi(r, t). \quad (14)$$

As the initial state we consider a one-dimensional Gaussian wave packet (3) with width parameter $\Sigma = 1.3836$ and phase space center $(q_0, p_0) = (4.53, 0)$, which corresponds to the initial data previously used for the analysis of a forward-backward IVR method²³ with the same potential.

2. The numerical setup

The reference solutions for the Schrödinger equation (14) are obtained by a high resolution Fourier split-step method with computational parameters listed in Table I. The final time 1668fs corresponds to roughly 836 time units with respect to the macroscopic time scale t/ε .

For the quasiclassical computation of expectation values, we sample the initial Wigner function with 10^5 Monte Carlo points, and perform the propagation with a time stepping

r interval	Fourier modes	time	timesteps
[3, 11]	$2 \cdot 10^4$	[0, 1668fs]	$2 \cdot 10^6$

Table I. Data of the reference solution for the vibrational Schrödinger equation (14) with $\varepsilon = 0.0122$.

$\tau = 4 \cdot 10^{-3}$ for the Störmer-Verlet integrator, see §IV B. Then we take the mean over ten independent runs of this setup.

For the computation of position densities according to §IV C, we use $4 \cdot 10^5$ Monte Carlo points in ten independent runs, a symplectic integrator¹⁹ of order eight with time stepping $\tau = 10^{-2}$, and 2^{12} Fourier modes for the inverse Fourier transform.

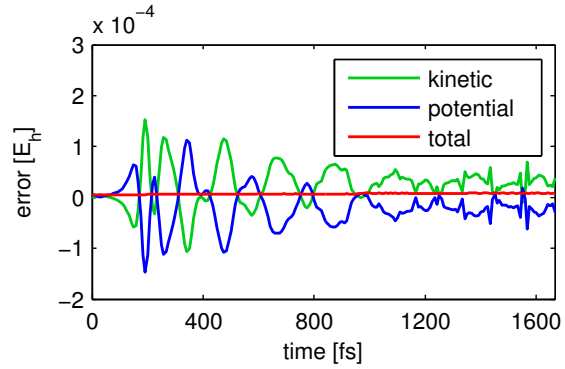


Figure 3. Evolution of the differences between the expected energies computed by the quasi-classical algorithm for the Iodine potential (13) and references obtained from highly accurate quantum mechanical calculations, see Table I.

3. Expectation values

The evolution of the kinetic, potential, and total energy errors from our numerical experiments is shown in Figure 3. It illustrates total energy conservation of the quasi-classical algorithm and shows small kinetic and potential energy errors over long times. Also for the evolution of the position and momentum expectation, the results of the quasi-classical algorithm

and the quantum mechanical references are very close, see Figure 4.

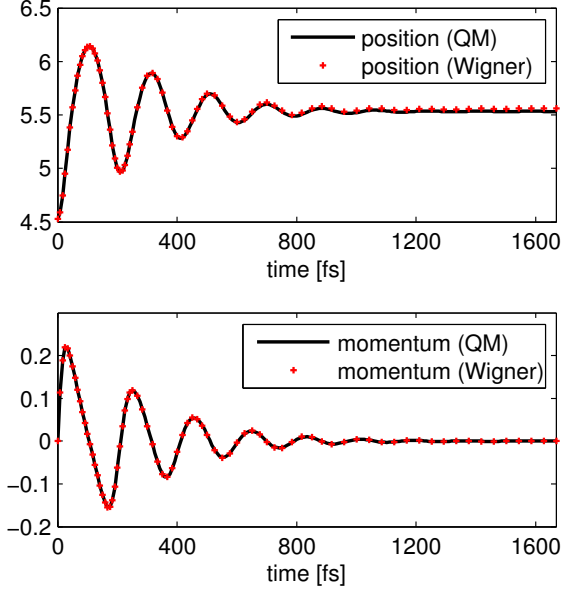


Figure 4. Evolution of the expected position and momentum in the I_2 system for both, the quasi-classical algorithm and quantum mechanical calculations.

In our simulations almost all of the classical trajectories are trapped in the Morse well, since the initial state is localized in the potential well with small kinetic energy. 99.57% of the Sobol points generated for the initial data lie within the trapping region, see the blue dots on top of the red contour lines in Figure 5. The stability and periodicity of the classical flow in this region imply that the error estimates of Egorov's theorem stay small up to times much longer than the uniform Ehrenfest timescale, see §II E.

4. Position densities

Lastly, we compare the quantum mechanical references $|(U_t\psi)(r)|^2 = |\psi_t(r)|^2$ with the approximative position densities $P_t(r)$. As in Ref.^{3,23} we show snap shots for different times,

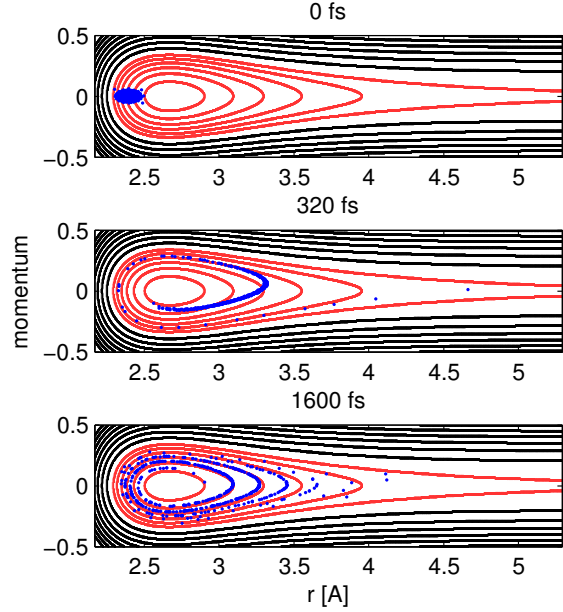


Figure 5. The dynamics of 500 initial sampling points superimposed on selected contour lines of the classical total energy. The red and black contours correspond to the trapping respectively unbounded energy region.

see Figure 6. Up to time 128fs, both position densities are almost indistinguishable. But also afterwards, even up to 1600fs, $P_t(r)$ represents a decent mean position density and displays the localization areas and strong peaks of the quantum mechanical position density better than expected.

To substantiate these observations, we introduce two different error measures, namely the integrated difference

$$E_1(t) = \int_0^\infty \left| |\psi_t(r)|^2 - P_t(r) \right| dr \quad (15)$$

and the maximal deviation of the cumulative distribution functions

$$E_c(t) = \sup_{x \geq 0} \left| \int_0^x (|\psi_t(r)|^2 - P_t(r)) dr \right|. \quad (16)$$

We always have

$$E_c(t) \leq E_1(t).$$

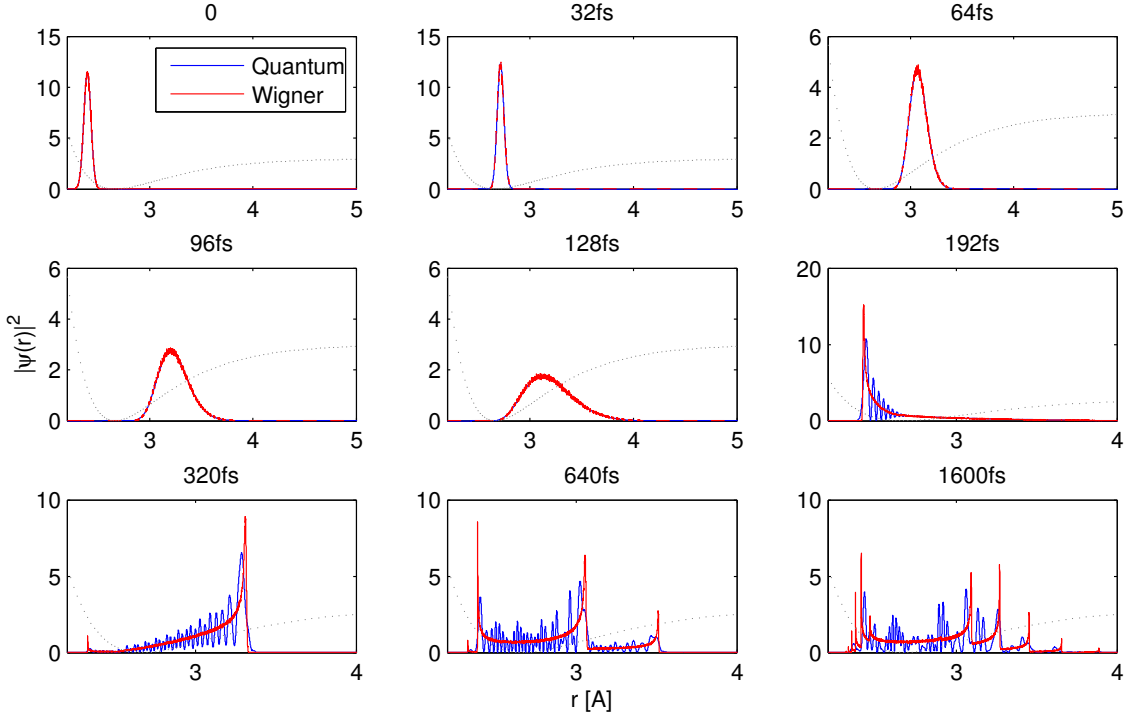


Figure 6. Quantum propagation and quasi-classical evolution of the position density for a Morse potential which corresponds to the electronic ground state of I_2 . The initial state is a Gaussian wavepacket centered at²³ $r = 2.4\text{\AA}$.

In our numerical experiments, however, the cumulative error is considerably smaller than the integrated one: Figure 7 shows that the inte-

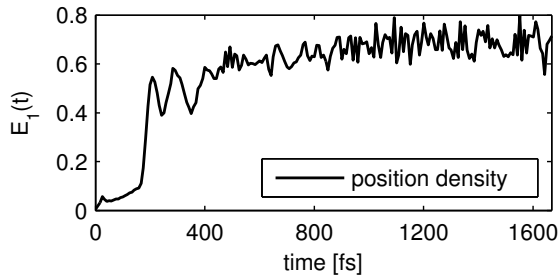


Figure 7. Evolution of the integrated difference (15) of the quasi-classical position density $P_t(r)$ and the reference density $|\psi_t(r)|^2$.

grated difference $E_1(t)$ stays small only until 170fs and deteriorates afterwards, illustrating the limitations of quasi-classical approximations as previously discussed in the literature^{3,6,23}. By contrast, Figure 8 displays the much smaller deviation of the cumulative distribution functions $E_c(t)$, which stays below $\sqrt{\varepsilon} \approx 0.11$ also for longer times, see §III A and Appendix C.

B. Henon-Heiles dynamics in higher dimensions

We present experiments with confined Henon-Heiles potentials^{24,25} in dimensions 2 to 32 which illustrate the performance of the quasi-classical algorithm in moderately high-dimensional situations.

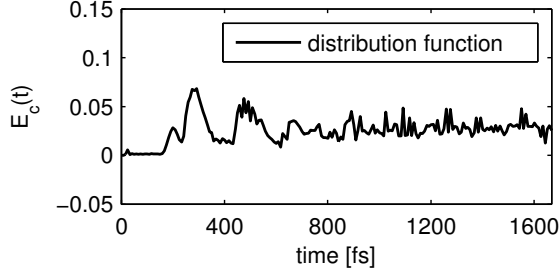


Figure 8. Evolution of the maximal deviation (16) of the cumulative position distribution functions associated with $P_t(r)$ and $|\psi_t(r)|^2$.

1. The model system

We investigate the dynamics of a hydrogen atom on a d -dimensional PES represented by the Henon-Heiles potential

$$\frac{m\phi^2}{2} \sum_{j=1}^d q_j^2 + \sigma \sum_{j=1}^{d-1} (q_j^2 q_{j+1} - \frac{1}{3} q_{j+1}^2)$$

with²⁶ $m = 1837m_e$, $\sigma = 0.0072E_h a_0^{-3}$, and $m\phi^2 = 0.0248m_e(\text{a.t.u.})^{-2}$. Rescaling space according to $q \mapsto q/\bar{q} = \sqrt{0.0248} q$, we obtain the semiclassical Schrödinger operator

$$\hat{H} = -\frac{\varepsilon^2}{2} \Delta + \frac{1}{2} \sum_{j=1}^d q_j^2 + 1.8436 \sum_{j=1}^{d-1} (q_j^2 q_{j+1} - \frac{1}{3} q_{j+1}^2)$$

with $\varepsilon = 0.0037$. Due to the large coupling constant 1.8436, the MCTDH calculations²⁶ for this Hamiltonian have employed complex absorbing potentials. Following Refs.^{24,25}, we do not add a complex absorber but a quartic confinement that prevents phase space trajectories from escaping to infinity. Our modified Henon-Heiles potential reads

$$V_d(q) = \frac{1}{2} \sum_{j=1}^d q_j^2 + 1.8436 \sum_{j=1}^{d-1} (q_j^2 q_{j+1} - \frac{1}{3} q_{j+1}^2) + 0.4 \sum_{j=1}^{d-1} (q_j^2 + q_{j+1}^2)^2. \quad (17)$$

As initial data²⁶ we consider the shifted harmonic ground state (3) of width $\Sigma = \text{Id}$, with initial position $q_{0,k} = 0.0408\text{nm}$ and initial momentum $p_{0,k} = 0$ for all $k = 1, \dots, d$. In the rescaled units, the shift equals $q_{0,k} \approx 0.1215\bar{q}$. With this choice of initial data, the total energy of the system grows with the dimension.

2. The numerical setup

In dimension $d = 2$, we compare the approximate expectation values of the kinetic, potential, and total energies obtained from the quasi-classical algorithm with reference data from a high resolution Strang splitting for the corresponding Schrödinger equation, see Table II. Because of the time rescaling, the final time of

space area	Fourier modes	time	timesteps
$[-5, 5] \times [-5, 5]$	2048×2048	$[0, 50]$	$5 \cdot 10^5$

Table II. Data of the reference solution of the vibrational Schrödinger equation for the 2-dimensional Henon-Heiles system, generated by a split step Fourier solver on the time interval $[0, 327\text{fs}]$.

$50/\varepsilon$ atomic time units equals 327fs. In dimensions $d > 2$ we restrict ourselves to the comparison of the evolution of potential energies, the preservation of the total energy and the computational effort.

For all classical trajectories, we used an symplectic integrator¹⁹ of order 8 with time stepping $\tau = 10^{-1}$.

3. Energy expectation values

Figure 9 shows the error of the quasi-classically computed expectation values of the total, potential and kinetic energy in dimension $d = 2$ with 2^{11} Sobol points. The errors are slightly larger than the ones obtained for the iodine system in Figure 3 but are below 10^{-3} up to the final time 327fs.

In Figure 10, we present the time-evolution of the potential energy for dimensions $d =$

$2, \dots, 32$ up to the shorter time 104fs. The results for a Monte Carlo sampling with 2^{14} normally distributed points or a Quasi-Monte Carlo sampling with 2^{12} Sobol points of the initial Wigner function are almost indistinguishable and show regular oscillations with roughly the same frequency in all dimensions. Also the total energy deviation in Figure 11 has regular oscillations, which are bounded by 10^{-10} as expected for a symplectic eighth order time discretization with step size $\tau = 10^{-1}$.

The computational times grow moderately with the dimension, reaching less than 20 seconds for the 32-dimensional case, see Table III.

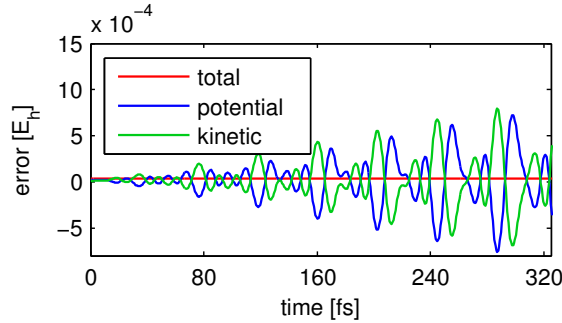


Figure 9. Differences between the expectation values of the energies obtained from the quasi-classical algorithm with $N = 2^{11}$ Sobol points and the references for the 2-dimensional Henon-Heiles system.

d	2	4	6	10	14	18	32
comp. time	0.7s	1.3s	2.0s	5.9s	7.7s	9.7s	19.8s

Table III. Computational time (in seconds) for the propagation of $N = 2^{12}$ Sobol points for the d -dimensional Henon-Heiles system up to 104fs.

4. Bath energy

Lastly, we revisit the dynamics for the 32-dimensional potential with slightly different initial data. As in Ref.²⁶, we view the last but four coordinates q_5, \dots, q_{32} as bath degrees of freedom, and use the initial harmonic ground state

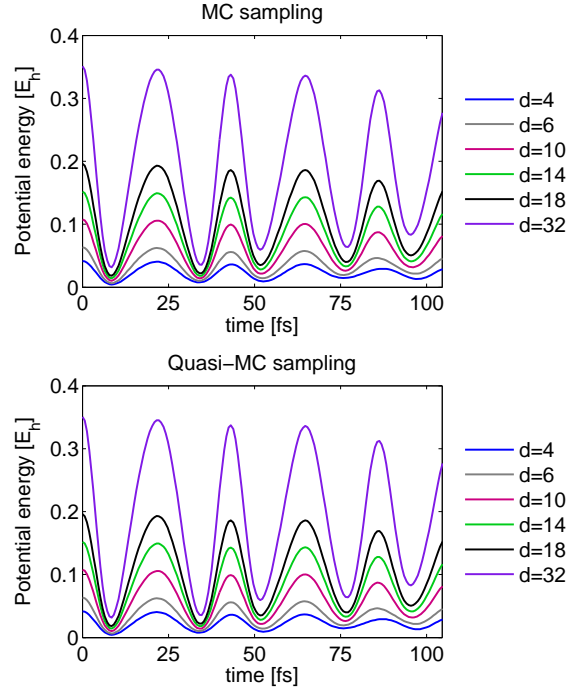


Figure 10. Evolution of the expected potential energies computed by the quasi-classical algorithm in dimensions 4 to 32.

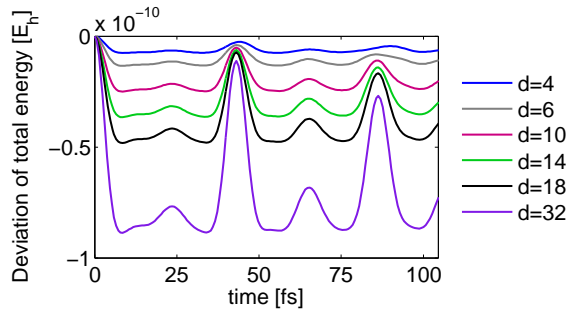


Figure 11. Deviation from the initial value of the total energy by the quasi-classical algorithm for dimensions 4 to 32.

with displacement $q_{0,k} \approx 0.1215\bar{q}$ only for the system coordinates $k = 1, \dots, 4$, while the bath degrees of freedom are localized at the origin.

We are interested in the evolution of the ex-

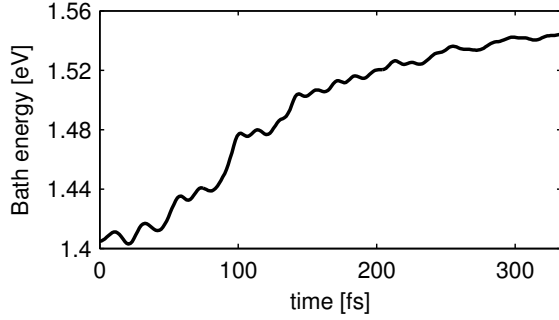


Figure 12. Quasi-classical evolution of the expected bath energy defined in (18).

pectation value of the bath energy

$$\begin{aligned} \widehat{H}_B = & \frac{1}{2} \sum_{j=5}^{32} (-\varepsilon^2 \partial_{q_j}^2 + q_j^2) + 0.9218 q_4^2 q_5 \\ & + 1.8436 \sum_{j=5}^{31} (q_j^2 q_{j+1} - \frac{1}{3} q_{j+1}^2), \quad (18) \end{aligned}$$

where the bath coupling term $1.8436 q_4^2 q_5$ has been divided equally between the system and the bath Hamiltonian. The quartic confinement or rather the missing complex absorbing potential in V_{32} does not allow for a quantitative comparison of the results in Figure 12 with the MCTDH calculations²⁶. Nevertheless, the qualitative structure and the range of the dynamics agree well. The bath energy computation for Figure 12 used 2^{12} Sobol points and took 63 seconds.

VI. CONCLUSION

We have related quasi-classical approximation schemes as the linearized semiclassical initial value representation (LSC-IVR) and the Wigner phase space method to Egorov's theorem. Depending on the quantity of interest, the error estimates may depend on the initial data: For the computation of typical expectation values, only normalized initial wave functions with $\langle \psi | \psi \rangle = 1$ are required for an error of

the order ε^2 . For the computation of position densities and transition probabilities, however, higher order derivatives of the initial Wigner function influence the accuracy of the approximation, such that for localized initial data the accuracy drops down to $\sqrt{\varepsilon}$. Our numerical experiments for a Morse model of diatomic iodine and for confined Henon–Heiles systems in various dimensions have illustrated the theoretical results but have also shown persistence on longer time scales than expected. The computational times are in the range of seconds.

VII. ACKNOWLEDGEMENTS

This research was supported by the German Research Foundation (DFG), Collaborative Research Center SFB-TRR 109, and the graduate program TopMath of the Elite Network of Bavaria.

Appendix A: Proof of Egorov's theorem

Egorov's theorem has a simple proof¹³, whose key element is the asymptotic expansion of the commutator of Weyl quantized observables in even powers of ε ,

$$\begin{aligned} \frac{i}{\varepsilon} [\widehat{A}, \widehat{B}] &= \frac{i}{\varepsilon} (\widehat{A}\widehat{B} - \widehat{B}\widehat{A}) \\ &\sim \sum_{k=0}^{\infty} \left(\frac{\varepsilon}{2i}\right)^{2k} \widehat{\{A, B\}}_{2k+1}, \end{aligned}$$

where the k th order Poisson bracket is defined according to

$$\{A, B\}_k = \sum_{|\alpha+\beta|=k} \frac{(-1)^{|\beta|}}{\alpha! \beta!} (\partial_q^\alpha \partial_p^\beta B) (\partial_q^\beta \partial_p^\alpha A).$$

One argues as follows:

$$\begin{aligned}
& U_{-t} \widehat{B} U_t - \widehat{B} \circ \widehat{\Phi}_t \\
&= \int_0^t \frac{d}{ds} \left(U_{-s} \widehat{B} \circ \widehat{\Phi}_{t-s} U_s \right) ds \\
&= \int_0^t U_{-s} \left(\frac{i}{\varepsilon} [\widehat{H}, \widehat{B} \circ \widehat{\Phi}_{t-s}] - \partial_t \widehat{B} \circ \widehat{\Phi}_{t-s} \right) U_s ds \\
&\sim \sum_{k=1}^{\infty} \left(\frac{\varepsilon}{2i} \right)^{2k} \int_0^t U_{-s} \text{op}(\{H, B \circ \Phi_{t-s}\}_{2k+1}) U_s ds,
\end{aligned}$$

with $\text{op}(A) = \widehat{A}$, since

$$\partial_t (B \circ \Phi_{t-s}) = \{H, B \circ \Phi_{t-s}\}_1.$$

The second order term

$$-\frac{\varepsilon^2}{4} \int_0^t U_{-s} \text{op}(\{H, B \circ \Phi_{t-s}\}_3) U_s ds$$

is expected to dominate the approximation error $E(V, B, \Phi_t)$ in Egorov's theorem (6).

Appendix B: Approximating position densities

In contrast to the LSC-IVR approximation error, which is uniform over all initial states with $\langle \psi | \psi \rangle = 1$, the accuracy of the quasi-classical computation of position densities¹⁶ by a combination of Egorov's theorem with the Fourier inversion formula depends on the initial state: The error of (8) is

$$\varepsilon^2 \langle \psi | \int E(V, B_\eta, \Phi_t) d\eta | \psi \rangle.$$

The dominant part of this term contains third order derivatives of the potential V and the observable B_η , that is,

$$\begin{aligned}
& \int_0^t \int \langle U_s \psi | \text{op}(\partial_q^3 V \partial_p^3 (B_\eta \circ \Phi_{t-s}) | U_s \psi) d\eta ds \\
&= \int_0^t \int W_s(z) \partial_q^3 V(q) \partial_p^3 (e^{-i\eta \cdot (q_{t-s} - r)}) dz d\eta ds \\
&= - \int_0^t \int (\partial_p^3 W_s)(\Phi_{s-t}(z)) (\partial_q^3 V)(q_{s-t}) \\
&\quad e^{-i\eta \cdot (q-r)} dz d\eta ds,
\end{aligned}$$

where W_s denotes the Wigner function of the time-evolved wave function $U_s \psi$. This implies, that the error is not uniform over all initial wave functions ψ with $\langle \psi | \psi \rangle = 1$, but crucially depends on third derivatives of its time-evolved Wigner function.

Appendix C: Heuristics for Wigner derivatives

We present a heuristic argument, explaining the considerable difference between the integrated error measure $E_1(t)$ and the cumulative measure $E_c(t)$ proposed in §V A 4.

If the initial state ψ is a vibrational Gaussian wavepacket (3), then there are Σ -dependent complex numbers $c_{m,n}$ such that

$$\partial_p^3 W_\psi = \varepsilon^{-3/2} \sum_{|(m,n)| \leq 3} c_{m,n} W(\psi_m, \psi_n),$$

where

$$\begin{aligned}
& W(\psi_m, \psi_n)(q, p) = \\
& (2\pi\varepsilon)^{-d} \int \psi_m(q - \frac{1}{2}y) \psi_n^*(q + \frac{1}{2}y) e^{ip \cdot y / \varepsilon} dy
\end{aligned}$$

denotes the joint Wigner function of two generalized coherent states^{14,27} ψ_m and ψ_n . We approximate

$$\begin{aligned}
& (\partial_p^3 W_s)(\Phi_{s-t})(z) \approx \\
& \varepsilon^{-3/2} \sum_{|(m,n)| \leq 3} c_{m,n} W(U_t \psi_m, U_t \psi_n)
\end{aligned}$$

and obtain

$$\begin{aligned}
& |(U_t \psi)(r)|^2 - P_t(r) \approx \\
& \sqrt{\varepsilon} F(V, \Phi_t) \sum_{|(m,n)| \leq 3} (U_t \psi_m)(r) (U_t \psi_n)(r)^*,
\end{aligned}$$

where $F(V, \Phi_t)$ depends on the potential V and the flow Φ_t . This implies for the two error measures

$$\begin{aligned}
& E_1(t) \approx \sqrt{\varepsilon} |F(V, \Phi_t)| \\
& \int_0^\infty \left| \sum_{|(m,n)| \geq 3} (U_t \psi_m)(r) (U_t \psi_n)(r)^* \right| dr
\end{aligned}$$

and

$$E_c(t) \approx \sqrt{\varepsilon} |F(V, \Phi_t)|$$

$$\sup_{x \geq 0} \left| \sum_{|(m,n)| \leq 3} \int_0^x (U_t \psi_m)(r) (U_t \psi_n)(r)^* dr \right|.$$

The decisive difference between the two error measures is therefore, that $E_1(t)$ depends on the integrated modulus of products of excited coherent states, whereas $E_c(t)$ sees the modulus of their cumulative overlap.

REFERENCES

- ¹W. Miller, J. Chem. Phys. **61**, 1823 (1974).
- ²H. Wang, X. Sun, and W. Miller, J. Chem. Phys. **108**, 9726 (1998).
- ³M. Thoss and H. Wang, Ann. Rev. Phys. Chem. **55**, 299 (2004).
- ⁴E. J. Heller, J. Chem. Phys. **65**, 1289 (1976).
- ⁵R. Brown and E. Heller, J. Chem. Phys. **75**, 186 (1981).
- ⁶M. Davis and E. Heller, J. Chem. Phys. **80**, 5036 (1984).
- ⁷H. Lee and M. Scully, J. Chem. Phys. **73**, 2238 (1980).
- ⁸X. Sun, H. Wang, and W. Miller, J. Chem. Phys. **109**, 4190 (1998).
- ⁹S. Habershon and D. Manolopoulos, J. Chem. Phys. **131**, 244518 (2009).
- ¹⁰Q. Shi and E. Geva, J. Chem. Phys. **118**, 8173 (2003).
- ¹¹J. Poulsen and P. Nyman, G Rossky, J. Chem. Phys. **119**, 12179 (2003).
- ¹²Y. Egorov, Uspekhi Mat. Nauk **24**, 235 (1969).
- ¹³A. Bouzouina and D. Robert, Duke Math. J. **111**, 223 (2002).
- ¹⁴C. Lasser and S. Troppmann, J. Fourier An. Appl. , 1 (2014).
- ¹⁵C. Lasser and S. Röblitz, SIAM J. Sci. Comput. **32**, 1465 (2010).
- ¹⁶X. Sun and W. Miller, J. Chem. Phys. **110**, 6635 (1999).
- ¹⁷S. Kube, C. Lasser, and M. Weber, J. Comput. Phys. **228**, 1947 (2009).
- ¹⁸J. Keller and C. Lasser, SIAM J. Appl. Math. **73**, 1557 (2013).
- ¹⁹H. Yoshida, Phys. Lett. A **150**, 262 (1990).
- ²⁰E. Hairer, C. Lubich, and G. Wanner, *Geometric numerical integration* (Springer, Heidelberg, 2010).
- ²¹R. F. Barrow and K. K. Yee, J. Chem. Soc., Faraday Trans. 2 **69**, 684 (1973).
- ²²J.-Y. Fang and C. C. Martens, J. Chem. Phys. **105**, 9072 (1996).
- ²³H. Wang, M. Thoss, K. L. Sørge, R. Gelabert, X. Gimenez, and W. H. Miller, J. Chem. Phys. **114**, 2562 (2001).
- ²⁴H.-D. Meyer, U. Manthe, and L. Cederbaum, Chem. Phys. Lett. **165**, 73 (1990).
- ²⁵A. Raab and H.-D. Meyer, J. Chem. Phys. **112**, 10718 (2000).
- ²⁶M. Nest and H.-D. Meyer, J. Chem. Phys. **117**, 10499 (2002).
- ²⁷G. Hagedorn, Ann. Phys. **269**, 77 (1998).